

Probing $WW\gamma$ coupling through $e^-\gamma \rightarrow \nu_e W^-$ at ILC

Satendra Kumar* and P. Poulouse†

Department of Physics, Indian Institute of Technology Guwahati, Guwahati 781 039, India

The anomalous $WW\gamma$ coupling is probed through $e\gamma \rightarrow \nu W$ at the ILC. With a spectacular single lepton final state, this process is well suited to study the above coupling. Cross section measurements can probe $\delta\kappa_\gamma$ to about ± 0.004 for a luminosity of 100 fb^{-1} at 500 GeV center-of-mass energy with unpolarized electron beam. The limits derivable on λ_γ from the total cross section are comparatively more relaxed. Exploiting the energy-angle double distribution of the secondary muons, kinematic regions sensitive to these couplings are identified. The derivable limit on $\lambda_\gamma < 0$ could be improved to a few per-mil, focusing on such regions. More importantly, the angular distributions at fixed energy values, and energy distribution at fixed angles present very interesting possibility of distinguishing the case of $\lambda_\gamma < 0$ and $\lambda_\gamma \geq 0$.

PACS numbers: 12.15.-y, 14.70.-e, 14.70.Fm, 14.65.Ha.

Keywords: Electron-Photon collision, γWW coupling, W-Boson, forward-backward asymmetry.

*Electronic address: satendra@iitg.ernet.in

†Electronic address: poulouse@iitg.ernet.in

I. INTRODUCTION

With the recent discovery of the Higgs boson by the LHC [1–4], the Standard Model (SM) has reaffirmed itself as the theoretical explanation of elementary particle dynamics, including presenting a plausible picture of Electroweak Symmetry Breaking (EWSB) [5, 6] through the Higgs mechanism. While this is so, and not withstanding the fact that SM has been extensively tested very successfully by many different experiments [7], it is widely believed that the SM is an effective theory, which needs to incorporate suitable modifications at large energies. Many expect that this large energy scale could be as small as a few TeV, which is being explored at the LHC. Apart from direct measurements of the properties of the Higgs boson, like its interaction couplings with itself, as well as with gauge bosons and fermions, signature of EWSB could be probed by understanding the structure and values of gauge-boson self interactions. This is so, because the longitudinal degrees of freedom of the gauge bosons arise from the Higgs sector. The relation between the Higgs-gauge boson couplings and the trilinear gauge couplings are presented and studied in Ref. [8, 9]. The discovery of Higgs boson of about 126 GeV mass, while establishing the Higgs mechanism as the method of EWSB, has opened an era of Higgs precision studies. Being a hadronic machine LHC has limitations to undertake precision studies. The International Linear Collider (ILC) proposed to collide high energy, high luminosity electrons and positrons has the mission of studying the SM at high precision and to look for signals beyond the standard model [10, 11]. Such a machine is well suited to an in-depth analysis of the gauge boson interactions within and beyond the SM. A large number of physics studies establish the fact that the potential of ILC is further enhanced by considering high energy photon-photon ($\gamma\gamma$) collisions as well as electron-photon ($e\gamma$) collisions, apart from the electron-positron (e^+e^-) collisions.

It is obvious that, the $e\gamma$ and $\gamma\gamma$ colliders are better suited to study the photon couplings with other gauge bosons like the γWW , $\gamma\gamma WW$, γZZ and $\gamma\gamma Z$ [12]. In this article we will focus on $e\gamma \rightarrow \nu W$ with $W \rightarrow l\bar{\nu}$. Signature of such an event is a single lepton with large missing energy. This process is sensitive to new physics effects including anomalous γWW [13, 14], composite fermion models [15], etc. In the case of anomalous γWW couplings, this process has the advantage over $e^+e^- \rightarrow W^+W^-$ [16], which is sensitive to both γWW and WWZ couplings. Again, $\gamma\gamma \rightarrow W^+W^-$ [17, 18] is sensitive to γWW , $\gamma\gamma WW$ and $\gamma\gamma Z$ couplings, revealing the edge of $e\gamma$ collider to study γWW . In most of the previous studies, observables at the production level of the single W is investigated, with the exception of Ref. [14], where the authors consider angular spectrum of the secondary leptons, also including the effect of off-shell W . Our main aim of this work is to study the possibility to exploit the secondary lepton spectrum including the energy and angular distributions to probe relevant new physics signals arising in anomalous γWW coupling.

In many models beyond the SM the quartic and triple-gauge boson couplings including γWW are altered from their SM values. In a model independent approach, an effective Lagrangian with terms additional to the SM Lagrangian is considered in phenomenological and experimental studies [19]. Relevant to the process considered here, the effective γWW vertex is commonly parametrized in terms of $\delta\kappa_\gamma$ and λ_γ , in the absence of CP violation (with vanishing SM values). LEP constraints in single-parameter analysis (taking one parameter at a time, keeping the others at their SM values) gives bounds of $-0.105 < \delta\kappa_\gamma < +0.069$, $-0.099 < \delta\kappa_\gamma < +0.066$ and $-0.059 < \lambda_\gamma < +0.026$, $-0.059 < \lambda_\gamma < +0.017$ and two-parameter analysis limits their values to $-0.072 < \delta\kappa_\gamma < +0.127$ and $-0.068 < \lambda_\gamma < +0.023$ [20, 21] at 95% C.L. Tevatron constraints from $W\gamma$ process are not contaminated by other couplings, but are more relaxed compared the LEP constraints to give $-0.51 < \delta\kappa_\gamma < +0.51$ and $-0.12 < \lambda_\gamma < +0.13$ [22]. The CMS constraints [23] from $W\gamma$ process are also more relaxed compared the LEP constraints.

Phenomenology of anomalous γWW coupling in the context of LHC as well as ILC has been carried out in a number of recent publications [13, 14, 24–26]. In particular, [14] has analyzed single W production with its leptonic decay to probe the effect of anomalous couplings in $e\gamma$ collision. In this work we exploit the full potential of the secondary lepton spectrum to study the effect of γWW coupling in $e\gamma \rightarrow \nu W \rightarrow \nu(l\bar{\nu})$.

In the next section we provide some details of the process and the observables used. In section 3 we present our numerical results, and finally summarize the study and present our conclusions in the last section.

II. ANALYSIS AND DISCUSSION

Considering a real on-shell photon, the most general CP-conserving γWW coupling within a Lorentz invariant Lagrangian can be written in the following form [19].

$$\mathcal{L}_{\gamma WW} = -ie \left[W_{\mu\nu}^\dagger W^\mu A^\nu - W_\mu^\dagger A_\nu W^{\mu\nu} + (1 + \delta\kappa_\gamma) W_\mu^\dagger W_\nu F^{\mu\nu} + \frac{\lambda_\gamma}{m_W^2} W_{\lambda\mu}^\dagger W_\nu^\mu F^{\lambda\nu} \right] \quad (1)$$

In the SM, the gauge structure $SU(2)_L \times U(1)_Y$ dictates the γWW couplings, with vanishing $\delta\kappa_\gamma$ and λ_γ at tree level. Therefore, precise measurements of these couplings will test the gauge sector of the electroweak interactions. Fig. 1 shows the Feynman diagrams for the process along with the momentum labels.

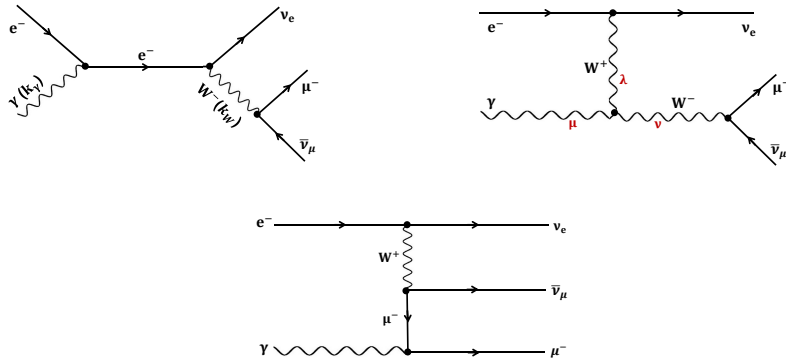


FIG. 1: Feynman diagrams for the process $e\gamma \rightarrow \nu W \rightarrow \nu(\mu\bar{\nu})$. First diagram shows the momenta used and second diagram shows the indices used in the vertex in Eq. 3

With the effective Lagrangian given by Eq. 1, the γWW vertex for the process under study (Fig. 1 (b)) takes the form:

$$\Gamma^{\mu\nu\lambda} = ie \left[2k_W^\mu g^{\nu\lambda} + 2k_\gamma^\nu g^{\mu\lambda} - (k_\gamma + k_W)^\lambda g^{\mu\nu} + (\delta\kappa_\gamma - \lambda_\gamma)(k_\gamma^\nu g^{\mu\lambda} - k_\gamma^\lambda g^{\mu\nu}) + \frac{\lambda_\gamma}{m_W^2} (k_\gamma + k_W)^\lambda (k_W^\mu k_\gamma^\nu - (k_\gamma \cdot k_W) g^{\mu\nu}) \right] \quad (2)$$

The effective Lagrangian in Eq. 1 should be considered as a low energy approximation of some fundamental theory, which is expected to emerge at some high energy scale, Λ . To control unitarity violation at high energies, we consider the anomalous couplings as form factors according to the following [14]

$$A = A_0 / \left[\left(1 + \frac{|k_W^2|}{\Lambda^2} \right) \left(1 + \frac{|(k_\gamma - k_W)^2|}{\Lambda^2} \right) \right], \quad (3)$$

where $A_0 \equiv \delta\kappa_\gamma, \lambda_\gamma$.

Contribution from the third diagram (Fig.1) is found to be a few percent, and will be neglected. This allows us to perform our computation in the Narrow-Width Approximation (NWA) in which the W -propagator is approximated to get

$$\frac{1}{|k_W^2 - m_W^2|^2} = \frac{\pi}{m_W \Gamma_W} \delta(k_W^2 - m_W^2), \quad (4)$$

where m_W is the mass and Γ_W is the width of the W boson.

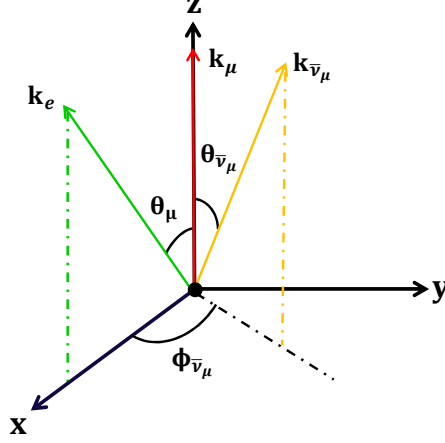


FIG. 2: Reference frame defining different momenta and corresponding angles used in Eq. 5.

To perform phase space integrations we fix our reference frame as the center-of-mass frame (CMF) of the colliding electron and photon system. z -axis is taken along \vec{k}_μ , which is the momentum of the outgoing lepton (considered as muon in the further discussion) as pictured in Fig. 2. y -axis is defined as $\vec{k}_\mu \times \vec{k}_e$, where \vec{k}_e is the momentum of the colliding electron. The $\bar{\nu}_\mu$ comes out at a polar angle $\theta_{\bar{\nu}_\mu}$ and azimuthal angle $\phi_{\bar{\nu}_\mu}$. Energy-momentum conservation and the NWA (Eq. 4) are used to get the differential cross-section

$$\frac{d\sigma}{dx_\mu d\cos\theta_\mu d\phi_{\bar{\nu}_\mu}} = \frac{x_\mu}{(2\pi)^3 128 m_W \Gamma_W} |M_r|^2, \quad (5)$$

where $x_\mu = \frac{2E_\mu}{\sqrt{\hat{s}}}$, with $\sqrt{\hat{s}}$ the center-of-mass energy and E_μ is the energy of the muon, and $\cos\theta_\mu = \frac{\vec{k}_\mu \cdot \vec{k}_e}{|\vec{k}_\mu| |\vec{k}_e|}$. Here M_r is the reduced amplitude given in terms of the invariant amplitude M as,

$$M = \frac{1}{(k_W^2 - m_W^2)} M_r. \quad (6)$$

$|M_r|^2$ is obtained using FORM computational package [27]. After integrating the unobservable $\phi_{\bar{\nu}_\mu}$, we get the double distribution of energy and polar angle of the secondary muon in the center-of-mass frame of the colliding particles with the electron momentum now taken along the redefined z axis. Notice that the muon energy in the CMF is bounded by $\frac{m_W^2}{2\sqrt{\hat{s}}} \leq E_\mu \leq \frac{\sqrt{\hat{s}}}{2}$.

To obtain the distribution in the lab frame, we need to boost the above differential cross-section appropriately. For an electron beam energy of E_e and photon energy of $\omega_\gamma = x E_e$, we have the following relation between the variables in the CMF and the laboratory frame.

$$\begin{aligned} \hat{s} &= x 4E_e^2 \\ E_\mu &= E_\mu^{lab} \gamma (1 - \beta \cos\theta_\mu^{lab}) \\ \cos\theta_\mu &= \frac{\cos\theta_\mu^{lab} - \beta}{1 - \beta \cos\theta_\mu^{lab}}, \end{aligned} \quad (7)$$

where β is the speed of the CMF compared to the lab frame, and $\gamma = \frac{1}{\sqrt{1-\beta^2}}$. Notice that the limits of E_μ^{lab} integration depends on $\cos\theta_\mu^{lab}$, keeping it within the bound

$$\frac{m_W^2}{4\sqrt{x}E_e} \frac{1}{\gamma (1 - \beta \cos\theta_\mu^{lab})} \leq E_\mu^{lab} \leq \frac{\sqrt{x}E_e}{\gamma (1 - \beta \cos\theta_\mu^{lab})}. \quad (8)$$

It is well known that the hard photons produced by Compton scattering are polarized. The polarization depends on the initial electron and laser beam polarizations. Besides, the final photon distribution will depend on the initial beam energies. Considering these, the parton level cross section need to be folded with the appropriate luminosity function, $\mathcal{L}_{e\gamma}(x)$, an expression for which is provided in the Appendix, so that the total cross-section in the lab frame is given by

$$\sigma = \int \frac{d\mathcal{L}_{\gamma/e}(x)}{dx} \sigma(\hat{s}) dx. \quad (9)$$

We suitably use Eqs. 5, 7, 12 to obtain the total cross-section, the muon angular distribution $\frac{d\sigma}{d\cos\theta_{\mu}^{lab}}$, the scaled muon energy distribution $\frac{d\sigma}{dx_{\mu}^{lab}}$, and the energy-angle distribution of the muons $\frac{d\sigma}{dx_{\mu}^{lab} d\cos\theta_{\mu}^{lab}}$ in the lab frame. Integrations over the photon distribution variable x , the scaled muon energy x_{μ}^{lab} and the muon angular variable $\cos\theta_{\mu}^{lab}$ in appropriate cases are performed numerically using the **Cuhre** routines under the **CUBA** package [28]. From now on we will drop the superscript *lab* from the variables.

Phenomenological analysis of $e\gamma \rightarrow \nu W$ is considered by some authors in the past [13, 14]. Most of the studies limit their analysis at the production level. Experimentally it is more useful to understand the effect on the final state particles arising from W decay. This is all the more important in the case of leptonic decay, as it is not possible to reconstruct the W in such case. In ref. [14], analysis including decay spectrum is presented, where detailed study of the secondary lepton angular distribution is considered along with other reconstructed observables concerning the W production. In the analysis presented here we demonstrate the usefulness of the combined energy-angle distribution of the secondary leptons in extracting information on the anomalous γWW couplings. While Ref. [14] takes into account the contribution due to off-shell W along with the on-shell production, our work is in the NWA assuming on-shell W production. At the same time, as note above, the effect of off-shell contribution, mainly arising through the diagram with muon propagator, is negligible, while the our analysis with energy-angle double distributions, along with combinations of the angular and energy distributions gives a handle on disentangling the effect of $\delta\kappa_{\gamma}$ and λ_{γ} , to certain extend.

III. NUMERICAL RESULTS

For our numerical analysis we consider ILC of center-of-mass energies of 500 GeV and 1000 GeV, with the option of $e\gamma$ collision using backscattered laser photons, and with unpolarized electron beams. It may be noted that as the process being considered is a purely a weak interaction process, only left-handed electrons will take part. Therefore, the left-polarized electron beam would enhance the cross-section, without presenting any additional advantage. We shall present all our analysis for unpolarized beam, without losing any generality.

Firstly, we consider the total cross-section. Fig. 3, shows the total cross-section against the center-of-mass energy of the $e^{-}e^{-}$ system (denoted as \sqrt{s}), one of which Compton-scatters on the laser beam to produce the high energy photon beam. The effect of $\delta\kappa_{\gamma}$ has an effect of about 7% to 8% almost all through the different center-of-mass energy values, while the effect of λ_{γ} has a dependence on the \sqrt{s} . This is expected, as the former is the coefficient of a dimension-4 operator, while the latter is the coefficient of a dimension-6 operator, thus producing a momentum dependence in the corresponding coupling. Again, for the same order of magnitudes of the couplings, the cross section is more sensitive to $\delta\kappa_{\gamma}$ compared to λ_{γ} , as expected for higher dimensional operators. One may note that the sensitivity to the sign of λ_{γ} ceases beyond the center-of-mass energies slightly beyond 500 GeV. This means that the effect of the interference term is overshadowed by the contribution purely coming from the dimension-6 anomalous term, which goes like the square of λ_{γ} . In order to be more quantitative, in Table I, we have presented the cross-sections for the limiting values of the couplings for two selected center-of-mass energy values, $\sqrt{s} = 500$ GeV and 1000 GeV. Taking individually separately, the effect of λ_{γ} is small, with a maximum of about 7% for negative values at 1000 GeV center-of-mass energy. It may be noted that the effect is sensitive to the sign of the parameter, indicating that the interference term is dominant, as expected. At 500 GeV, one can ignore the effects of λ_{γ} even when considering along with $\delta\kappa_{\gamma}$, whereas at 1000

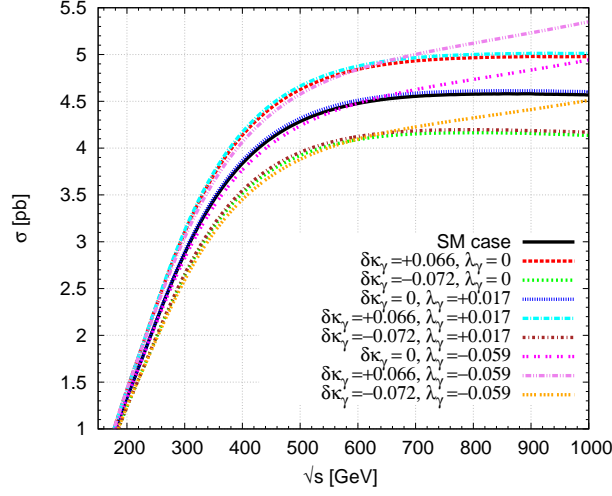


FIG. 3: Total cross-section against $\sqrt{s} = 2E_e$, where E_e is the electron beam energy, for different anomalous couplings, along with the SM case.

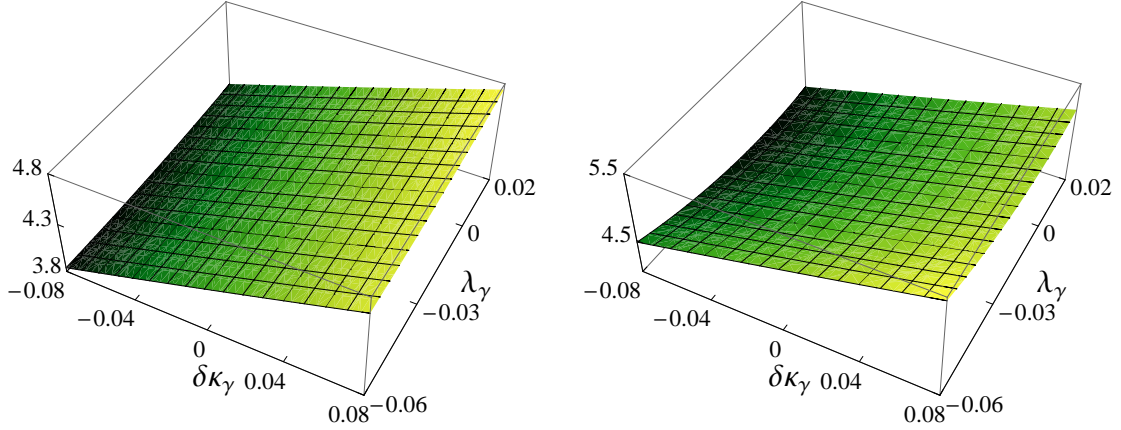


FIG. 4: The surface plots showing the total cross-section against $\delta\kappa_\gamma$ and λ_γ for the center-of-mass energy (\sqrt{s}) of 500 GeV (left) and 1000 GeV (right), where cross-section in pb is along the vertical axis.

GeV, the presence of λ_γ can either nullify or enhance considerably the effect of $\delta\kappa_\gamma$. Largest effect is seen when $\delta\kappa_\gamma$ is positive and λ_γ is negative, with about 20% deviation in the total cross-section at 1000 GeV. In the surface plots shown in Fig.4, variation of the cross-section with $\delta\kappa_\gamma$ and λ_γ at center-of-mass energy of 500 GeV and 1000 GeV are presented, which show monotonous dependences, almost a linear one, as expected from the fact that only the interference terms play role. We shall see below that, with such large cross-section, small deviations even at percent or sub-percent level will be able to probe the relevant parameters significantly.

The two-parameter bound showing the allowed region in the $\delta\kappa_\gamma - \lambda_\gamma$ plane is presented in Fig.5, at center-of-mass energy of 500 GeV with an integrated luminosity of 100 fb^{-1} . This corresponds to number of event of about 430000. Thus, with the dependence described above, the reach on the parameters for these machine parameters is expected to be very good. We remind the reader that, when cross-section is considered as a function of anomalous coupling parameters $\delta\kappa_\gamma$ and λ_γ , the

$\delta\kappa_\gamma,$	λ_γ	σ [pb]	
		$\sqrt{s} = 500$ GeV	$\sqrt{s} = 1000$ GeV
SM case		4.284	4.568
+0.066,	0	4.626	4.977
-0.072,	0	3.922	4.135
0,	+0.017	4.319	4.602
0,	-0.059	4.238	4.942
+0.066,	+0.017	4.662	5.012
+0.066,	-0.059	4.576	5.350
-0.072,	+0.017	3.955	4.169
-0.072,	-0.059	3.879	4.510

TABLE I: Total cross-section for different combinations of TGC parameters at $\sqrt{s} = 500$ GeV and 1000 GeV.

result is a second order polynomial in these two parameters. With this, the 3σ limit of the cross-section leads to an elliptic equation corresponding to the relation between these two parameters. This results in an elliptic band in the $\delta\kappa_\gamma - \lambda_\gamma$ plane respecting the 3σ limit of the cross-section. Very strong bound on $\delta\kappa_\gamma$ can be derived for any assumed value of λ_γ . On the other hand, for small values of $\delta\kappa_\gamma$ the sensitivity of cross-section on λ_γ is comparatively smaller. At the same time, the relative sign of the parameters is preferred to be opposite to each other, as was also evident from the analysis above.

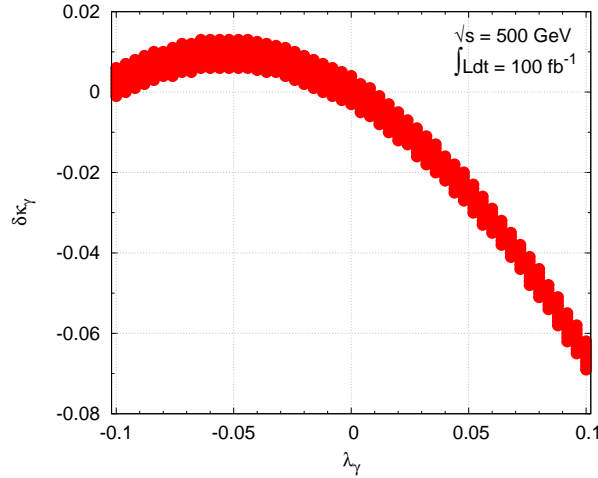


FIG. 5: The shaded region corresponds to values of $\delta\kappa_\gamma - \lambda_\gamma$ with the total cross-section within the 3σ limit, for an integrated luminosity of 100 fb^{-1} at a center-of-mass energy of 500 GeV.

Moving on to the single parameter, sensitivity of cross-section on one parameter, while the other one is fixed is presented in Fig. 6, for center-of-mass energies of 500 GeV and 1000 GeV. The green band represents the 3σ region of the SM value of the cross-section, considering an integrated luminosity of 100 fb^{-1} . The cross-section has a linear dependence on $\delta\kappa_\gamma$, showing that the contribution proportional to the quadratic term is negligible. The 3σ allowed range of $\delta\kappa_\gamma$ shifts with the value of λ_γ . Although, as Table I suggests, the effect of λ_γ is small compared to the large effect of $\delta\kappa_\gamma$ values, the influence is significant for derivable limits as can be read from Fig. 6. For example, at 500 GeV center-of-mass energy, assuming $\lambda_\gamma = 0$, one obtains a 3σ limit of $-0.004 \leq \delta\kappa_\gamma \leq +0.004$, which is moved to about $-0.008 \leq \delta\kappa_\gamma \leq 0$ for $\lambda_\gamma = 0.01$, or

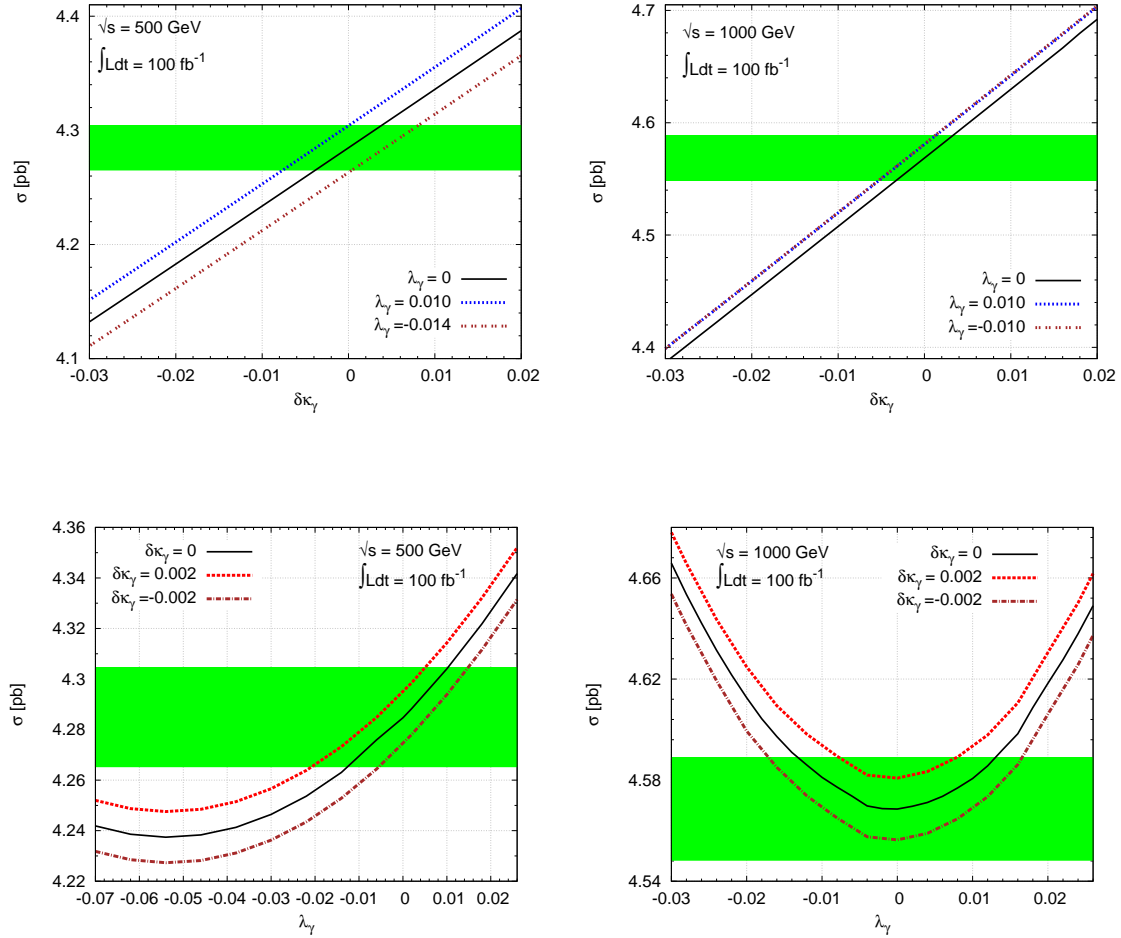


FIG. 6: Cross-section against $\delta\kappa_\gamma$ (top row) and λ_γ (bottom row), when the other parameter assume typical values. The center-of-mass energies considered are $\sqrt{s} = 500$ GeV (left column) and 1000 GeV (right column). The green band indicates the 3σ limit of the SM cross-section, with integrated luminosity of 100 fb^{-1} .

moved to $0 \leq \delta\kappa_\gamma \leq +0.008$ for $\lambda_\gamma = -0.014$. In the case of 1000 GeV center-of-mass energy, the cross-section is not sensitive to the sign of λ_γ , as already discussed. Thus, the deviation of the dependence of the cross-section of λ_γ from linearity is evidently seen in Fig. 6 (lower right). On the other hand, in the case of λ_γ , at 500 GeV with 100 fb^{-1} , and keeping $\delta\kappa_\gamma = 0$, a limit of $-0.013 \leq \lambda_\gamma \leq +0.01$ could be reached, which is changed to $-0.02 \leq \lambda_\gamma \leq +0.004$ if $\delta\kappa_\gamma = +0.002$, and $-0.005 \leq \lambda_\gamma \leq +0.015$ if $\delta\kappa_\gamma = -0.002$. In the case of 1000 GeV center-of-mass energy, the reach on λ_γ are $-0.013 \leq \lambda_\gamma \leq +0.013$, $-0.008 \leq \lambda_\gamma \leq +0.008$ and $-0.017 \leq \lambda_\gamma \leq +0.017$ corresponding to $\delta\kappa_\gamma = 0$, $+0.002$ and -0.002 , respectively. Thus, quite evidently, the study of the cross-section alone will not provide information regarding the values of or reach of either of the parameters in question. Possibilities of disentangling these effects will be discussed through a study of different kinematic distributions of the decay products.

We next consider the angular distribution of the secondary muons plotted in Fig. 7 for different combinations of $\delta\kappa_\gamma$ and λ_γ , at center-of-mass energies of 500 GeV and 1000 GeV. As can be seen, the effect is more pronounced at smaller $\cos\theta_\mu$ values, while most of the events are gathered in the forward direction. With high luminosity, one can expect high statistics for single W production at $e\gamma$ collider. This means, that either the entire backward region, or even a smaller region of the

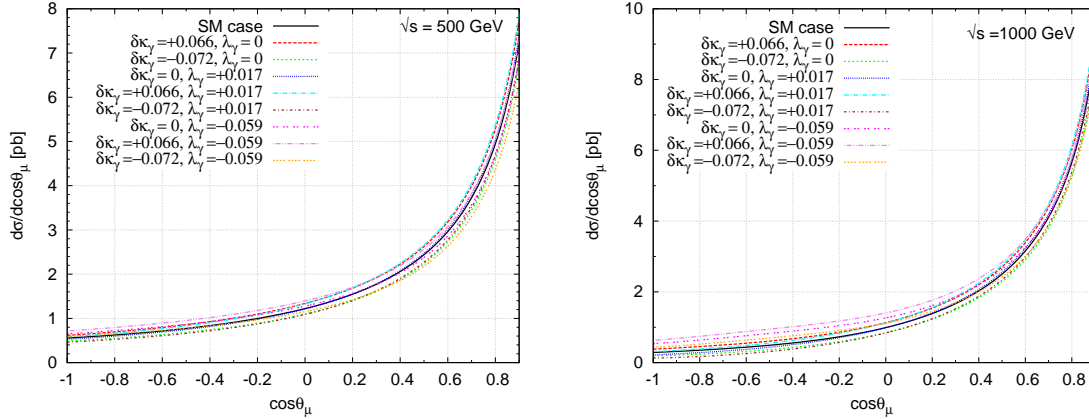


FIG. 7: The angular distribution for different combinations of $\delta\kappa_\gamma$ and λ_γ for the two different values of $\sqrt{s} = 500$ GeV (left) and 1000 GeV (right).

$\cos\theta_\mu$ could be probed to see the effect of anomalous TGC. In Table II the deviation from SM case is illustrated by considering a bin of $-0.90 \leq \cos\theta_\mu \leq -0.85$ with an integrated luminosity of 100 fb^{-1} . The number of events in the backward hemisphere (N^{back}), and the deviation from the SM case ($\Delta^{\text{back}} = N^{\text{back}} - N_{\text{SM}}^{\text{back}}$) show that deviations as big as 30% is possible in at $\sqrt{s} = 500$ GeV, which is increased to close to 150% at $\sqrt{s} = 1000$ GeV. The deviations are more pronounced in the case of 1000 GeV, compared to 500 GeV. The large sensitivity of this observable to the different combinations of the two anomalous couplings gives a way to distinguish different scenarios. A very moderate luminosity of 100fb^{-1} gives enough statistics to mean that 10% deviation correspond to 5 - 6 σ deviation. Another way to present this effect is through the forward-backward asymmetry, defined as

$$A_{FB}^a = \frac{\left[\int_{-1}^0 \frac{d\sigma}{d\cos\theta_\mu} d\cos\theta_\mu - \int_0^1 \frac{d\sigma}{d\cos\theta_\mu} d\cos\theta_\mu \right]}{\left[\int_{-1}^0 \frac{d\sigma}{d\cos\theta_\mu} d\cos\theta_\mu + \int_0^1 \frac{d\sigma}{d\cos\theta_\mu} d\cos\theta_\mu \right]},$$

$$\Delta A_{FB}(\%) = \frac{|A_{FB}^{\text{Ano.}} - A_{FB}^{\text{SM}}|}{A_{FB}^{\text{SM}}} \times 100. \quad (10)$$

In Fig. 8, this asymmetry is presented for different combinations of the parameter values. In the SM, at 1000 GeV with 100 fb^{-1} integrated luminosity, we expect about 460000 number of events in total (with 100% efficiency of detection). Out of this, about 380000 is expected to be in the forward direction giving rise to an asymmetric number of events of about 300000. Considering the statistical uncertainty, even a deviation at a few percent level is perceivable. We have considered a typical 1% deviation to find the reach of the couplings for this configuration of the collider. The green band shows the region that falls within 1% deviation from the SM values. The single parameter reach on $\delta\kappa_\gamma$ is better through the consideration of cross-section compared to the forward-backward asymmetry. On the other hand, the case of λ_γ is quite different. At $\sqrt{s} = 1000$ GeV, the reach could be improved by factor of 2 to $-0.005 \leq \lambda_\gamma \leq +0.005$. More importantly, the dependence of the derivable limits, which was about 30% in the case of the limits drawn from the cross-section, is now reduced to about 10% at this center-of-mass energy, clearly demonstrating the advantage of the A_{FB} in probing the influence of λ_γ .

So far, we have noted the influence of one of the couplings in deriving the bound on the other. In order to see the possibility of disentangling the effects of these couplings, we shall turn to the

$\delta\kappa_\gamma$	λ_γ	$\sqrt{s} = 500 \text{ GeV}$		$\sqrt{s} = 1000 \text{ GeV}$	
		N^{back}	$\Delta^{\text{back}} \%$	N^{back}	$\Delta^{\text{back}} \%$
SM case		2900	0	1600	0
0.066	0	3250	12	2100	31
-0.072	0	2600	-10	1100	-31
0	0.017	2800	-3	1250	-22
0	-0.059	3400	17	2850	78
0.066	0.017	3100	7	1700	6
0.066	-0.059	3750	30	3900	144
-0.072	0.017	2400	-17	750	-53
-0.072	-0.059	3050	5	2350	43

TABLE II: The number of events within $-0.90 \leq \cos \theta_\mu \leq -0.85$ for different combinations of $\delta\kappa_\gamma$ and λ_γ at $\sqrt{s} = 500 \text{ GeV}$ and 1000 GeV , along with the corresponding deviation from the SM case. An integrated luminosity of 100 fb^{-1} is considered.

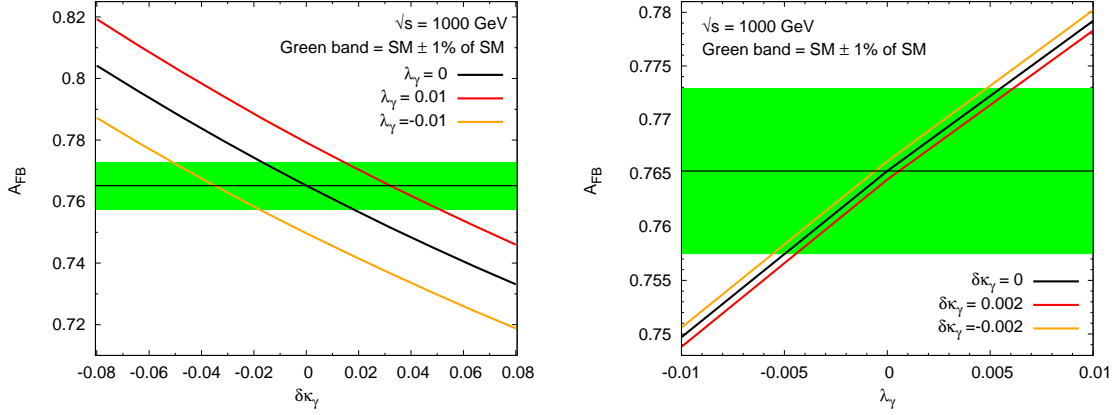


FIG. 8: The forward-backward asymmetry against $\delta\kappa_\gamma$ (top row) and λ_γ (bottom row) at $\sqrt{s} = 500 \text{ GeV}$ (left) and 1000 GeV (right). The green band correspond to a $\pm 10\%$ deviation from the SM case.

kinematic distributions like the energy distribution, alone and in combination with the angular distribution. In Fig.9, the energy distribution against $x_\mu = \frac{E_\mu}{E_e}$, where E_e is the electron beam energy is presented, showing the effect of anomalous couplings for different combination of TGC parameters at \sqrt{s} of 500 GeV and 1000 GeV . Once again, we emphasize that it is only through a combination of different observables that one may be able to disentangle information regarding the $\delta\kappa_\gamma$ and λ_γ couplings. The influence of $\delta\kappa_\gamma$ remains more or less the same throughout the range of x_μ . At the same time, $\lambda_\gamma > 0$ has a slight diminishing effect in the low energy region, and a slight enlarging effect at the high energy region. On the other hand, $\lambda_\gamma < 0$ has a large enlarging effect at low energies, which turns the other way around, but with a much smaller magnitude at higher energies. Thus, the energy distribution of the secondary muons become a clear discriminator of these qualitatively different scenarios, as summarized in Table III.

A more detailed picture could be made available by exploiting the energy-angle double distribution, as presented in Fig. 10, where the SM distribution (top left) and the deviations from the SM in the presence of $\delta\kappa_\gamma$ and λ_γ , individually, are shown. Deviation in the case of $\lambda_\gamma > 0$ is negligible, and therefore not presented. Evidently, in order to probe λ_γ , one need to focus on the low energy

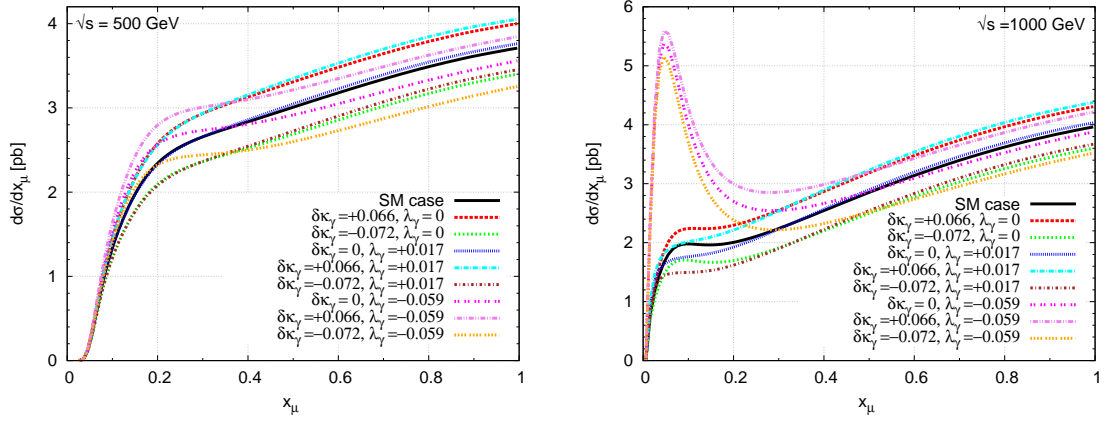


FIG. 9: The energy distribution of the secondary muon for different combinations of $\delta\kappa_\gamma$ and λ_γ , compared with the SM case. Center-of-mass energies considered are $\sqrt{s} = 500$ GeV (left) and 1000 GeV (right).

Scenario	Effect on μ energy
$\delta\kappa_\gamma > 0$	enhancing effect
$\lambda_\gamma \geq 0$	both low and high energies
$\delta\kappa_\gamma < 0$	diminishing effect
$\lambda_\gamma \leq 0$	both low and high energies
$\delta\kappa_\gamma \geq 0$	large enhancing effect at low energies
$\lambda_\gamma < 0$	diminishing effect at high energies, depending on $\delta\kappa_\gamma$
$\delta\kappa_\gamma < 0$	large enhancing effect at low energies
$\lambda_\gamma < 0$	small enhancing effect at high energies, depending on $\delta\kappa_\gamma$

TABLE III: Disentangling different scenarios based on the energy distribution of the secondary μ .

muon emerging in the backward region, with with some trace in the high energy - backward region, and very low energy forward region. On the other hand, the signature of $\delta\kappa_\gamma$ will be seen more visibly in the forward direction for high energy μ . In the case of low energy μ , the effect of $\delta\kappa_\gamma$ is somewhat independent of the angle, except for the extreme forward region. The reason for these complex dependence is a result of the complex interdependence of the kinematic variables and the parameters, the origin of which are difficult to decipher,.

Taking slices from the above surface plots, the energy distributions at fixed angles of 60° and 150° are presented in Fig. 11 corresponding to center-of-mass energy of 1000 GeV. These angles represent the typical behaviour in the low and high angle regions, respectively. Quantifying these effects, the number of events in the chosen energy bins for the above angles, corresponding to the SM case as well as different combinations of the anomalous couplings, along with the percentage deviations is given in Table IV. The energy bins are chosen to maximize the effect, in each case. In the forward region with high energy muon, where the effect of λ_γ is small, whereas the $\delta\kappa_\gamma$ has large effects has a maximum of 12% in the case of $\sqrt{s} = 500$ GeV, which remains more or less at the same level (10%) in the case of $\sqrt{s} = 1000$ GeV. On the other hand, the presence of λ_γ has much larger impact, with 33% when $\delta\kappa_\gamma$ is zero at $\sqrt{s} = 500$ GeV, which is increased to 41% along with positive values of $\delta\kappa_\gamma$ and decreased to 21% for its negative values. These effects can

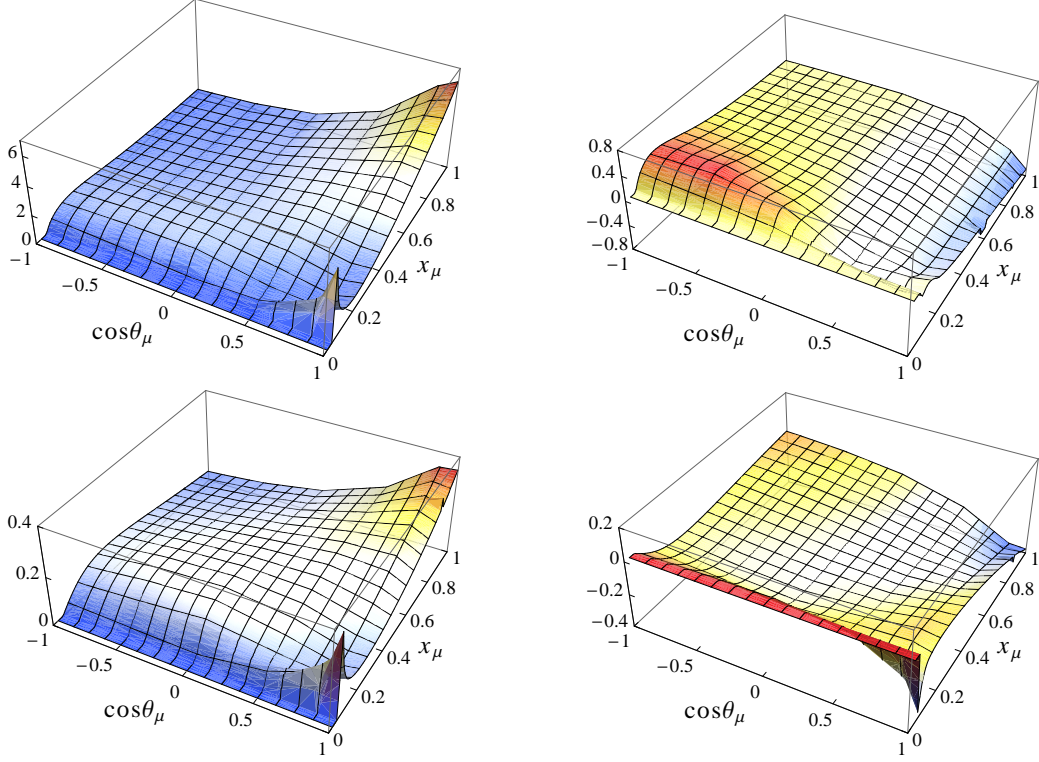


FIG. 10: The energy-angle double distribution of the secondary muon (along the vertical axis: $\frac{d\sigma}{dx_\mu d \cos \theta_\mu}$ (pb)) at $\sqrt{s} = 500$ GeV. Top left is the SM case. Other cases are deviations from the SM; $\delta\kappa_\gamma = 0$, $\lambda_\gamma = -0.059$ (top right); $\delta\kappa_\gamma = +0.069$, $\lambda_\gamma = 0$ (bottom left); $\delta\kappa_\gamma = -0.072$, $\lambda_\gamma = 0$ (bottom right).

$\delta\kappa_\gamma$ λ_γ	$\sqrt{s} = 500$ GeV				$\sqrt{s} = 1000$ GeV			
	$\theta_\mu = 60^\circ$		$\theta_\mu = 150^\circ$		$\theta_\mu = 60^\circ$		$\theta_\mu = 150^\circ$	
	$x_\mu = 0.95 - 1.0$		$x_\mu = 0.056 - 0.106$		$x_\mu = 0.95 - 1.0$		$x_\mu = 0.056 - 0.106$	
	N_{events}	Δ [%]	N_{events}	Δ [%]	N_{events}	Δ [%]	N_{events}	Δ [%]
SM Case	13500	—	6200	—	14750	0	6000	0
0.066 0	14550	8	6750	9	15900	8	7000	17
-0.072 0	12450	-8	5650	-9	13600	-8	5000	-17
0 0.017	13750	2	5750	-7	15000	2	4000	-33
0 -0.059	13000	-4	8250	33	14500	-2	14500	141
0.066 0.017	14750	9	6250	1	16225	10	4750	-21
0.066 -0.059	14000	4	8750	41	15600	6	15500	158
-0.072 0.017	12650	-6	5250	-15	13850	-6	3000	-50
-0.072 -0.059	11900	-12	7500	21	13300	-10	13400	123

TABLE IV: The number of events within specified x_μ bins, and for fixed θ_μ , for different combinations of $\delta\kappa_\gamma$ and λ_γ at $\sqrt{s} = 500$ GeV and 1000 GeV, along with the corresponding percentage deviation (Δ) from the SM case. An integrated luminosity of 100fb^{-1} is considered.

be increased to more than 4 times for $\sqrt{s} = 1000$ GeV.

Focusing on the low energy region, we consider variation with θ_μ for fixed $x_\mu = 0.2$ (as a typical value), and present difference scenarios in Fig. 12. While the absence of λ_γ and its positive values

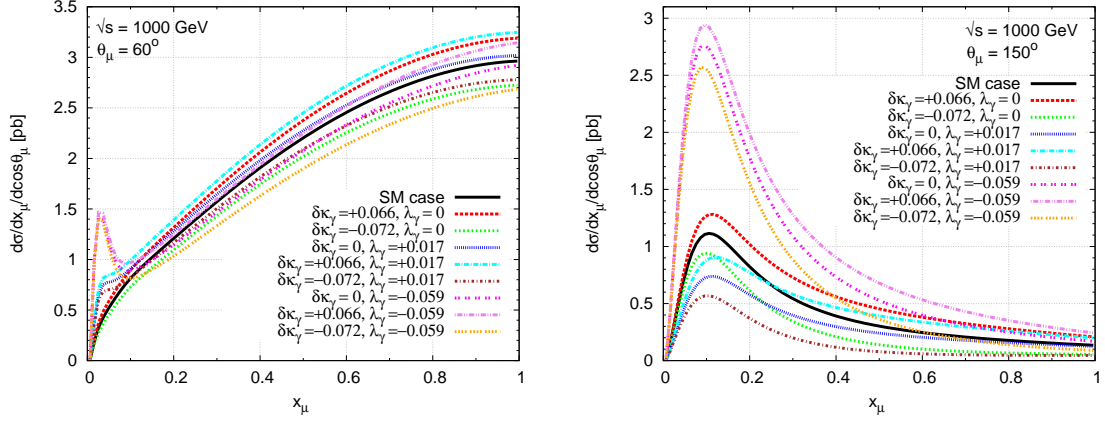


FIG. 11: The energy distribution of the secondary muon for different combinations of $\delta\kappa_\gamma$ and λ_γ , considered at muon angles of $\theta_\mu = 60^\circ$ and 150° , at $\sqrt{s} = 1000$ GeV.

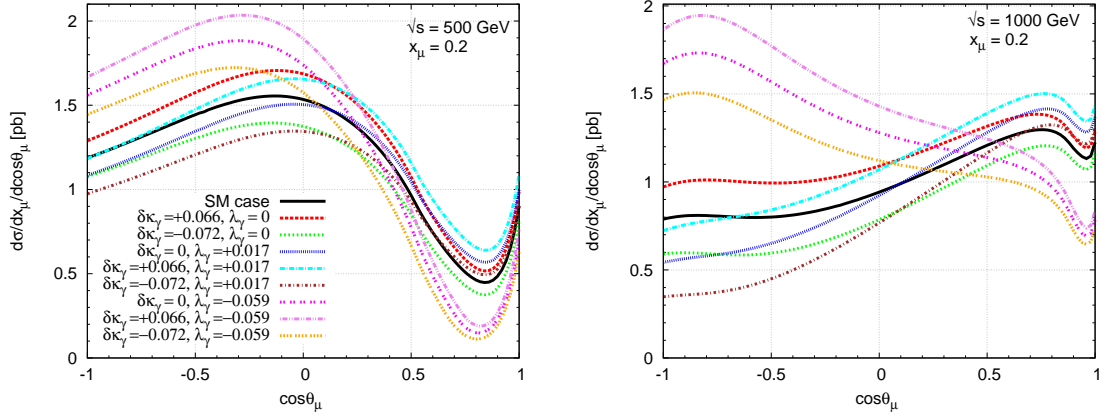


FIG. 12: The energy-angle distribution of the secondary muon for different combinations of $\delta\kappa_\gamma$ and λ_γ , considered at fixed muon energy parameter (x_μ) at \sqrt{s} of 500 GeV and 1000 GeV. Colour coding is the same in all plots.

for different $\delta\kappa_\gamma$ values have moderate impact, especially in the backward region, the negative values of λ_γ could produce significantly different distributions. In order to quantify the effects, we have computed the forward-backward asymmetry in each of these cases, and tabulated in Table V. The deviations are evidently more pronounced in all cases, and much larger in the $\lambda_\gamma \leq 0$ case. Note that owing to large cross-section, even limiting to a small energy bin of $\Delta x_\mu = 0.2$ around the μ energy considered will lead to about 40000 events, when integrated over the angle. Thus, a change in the forward-backward asymmetry to the tune of 200% is certainly detectable. Coming to the reach on the value of the couplings achieved through these observations, we note that the asymmetry in the SM case is about -19% , and $+40\%$ at $\sqrt{s} = 500$ GeV and 1000 GeV, respectively. We summarize the extend of asymmetry measurement in Table VI, considering purely statistical uncertainty. This suggests that deviations from the asymmetry of about 5 % could be expected at 3σ level for . Reading it along side Table V indicates a reach of about an order of magnitude better than that the value considered there, which means about $\lambda_\gamma \sim -0.003$, assuming a linear dependence.

$\delta\kappa_\gamma$	λ_γ	$\Delta A_{FB}(\%)$	
		$\sqrt{s} = 500 \text{ GeV}$	$\sqrt{s} = 1000 \text{ GeV}$
0.066	0	-4	-33
-0.072	0	5	48
0	0.017	-34	72
0	-0.059	92	-205
0.066	0.017	-36	29
0.066	-0.059	83	-213
-0.072	0.017	-32	135
-0.072	-0.059	102	-194
SM case; $A_{FB} =$		-0.185	0.398

TABLE V: Observed forward-backward asymmetry and its deviation from the SM with a fixed muon energy corresponding to $x_\mu = 0.2$, at $\sqrt{s} = 500$ and 1000 GeV.

	N^F	N^B	$A^{FB} \%$	$\Delta A^{FB} \%$	reach on λ_γ at $(3 \times \Delta A^{FB})$ level
SM	18000	26000	18.5		
$N^i \pm \sqrt{N^i}$	[17866,18134]	[25839,26161]	[17.5,18.8]	[-5.0,+1.6]	-0.003

TABLE VI: Number of events in the forward (N^F) and backward (N^B) hemispheres, and the corresponding forward-backward asymmetry (A^{FB}) in the case of the SM with a fixed muon energy of 50 GeV (corresponding to $x_\mu = 0.2$) considering a bin of $\Delta x_\mu = 0.2$ ($\Delta E_\mu = 50 \text{ GeV}$), at $\sqrt{s} = 500 \text{ GeV}$ and luminosity of 100 fb^{-1} .

IV. SUMMARY AND CONCLUSIONS

With the W decaying into muons, the single W production in $e\gamma$ collisions has a spectacular final state of one single muon, and missing energy. The process is well suited to study the $WW\gamma$ coupling. It may be noted that the process has the advantage that, unlike other relevant process like the W pair production at e^+e^- collisions, it is devoid of effects from other anomalous couplings like WWZ . Considering this process, angular distribution of secondary muons in the lab frame is easily constructed, and is readily available in the literature. At the same time, such is not the case of its energy distribution. Here we have presented a semi-analytical way to explore the secondary lepton energy-angle distributions in $e\gamma \rightarrow \nu W$ with $W \rightarrow l\bar{\nu}$. The advantage of such an observable in analyzing the SM case and probing possible new physics effects is demonstrated. Variables being defined in the lab frame, are directly used to probe different kinematic regions, so as to explore the sensitivity of the anomalous couplings.

We have derived possible limits on the anomalous couplings $\delta\kappa_\gamma$ and λ_γ , which may be obtained from the cross-section measurements. It is shown that, assuming the other couplings is absent, 3σ level of cross-section can probe $\delta\kappa_\gamma$ to the level of ± 0.004 , and constrain λ_γ to $-0.013 \leq \lambda_\gamma \leq +0.01$, for a moderate luminosity of 100 fb^{-1} at a center-of-mass energy of 500 GeV. The large influence of each of these couplings on the sensitivity of the other is quite visible in the derivable limits. Scanning the two parameter plane the 3σ bound is presented, showing that $\delta\kappa_\gamma$ could be bounded to small regions for particular values of λ_γ . The angular distributions along with forward-backward asymmetry improve the situation with better sensitivity. With the large cross-section, the statistics is very good even for 100 fb^{-1} integrated luminosity, which could measure the forward-backward asymmetry to a few percent level. It is found that this could be utilized to improve the limits on λ_γ , whereas not so in the case of $\delta\kappa_\gamma$. Exploring different kinematic regions, and studying suitably constructed observables would be able to distinguish different scenarios

involving the couplings. We studied the energy and angle distributions of the μ separately and together to understand how these could be fruitfully employed for this purpose. The energy-angle double distribution enables one to identify the kinematic regions sensitive to different couplings, and their signs. We have found that focusing on the low energy μ in the backward direction are more sensitive to the case of $\lambda_\gamma < 0$, whereas the $\delta\kappa_\gamma$ does not show distinguishable preference to the kinematic regions. Our analysis shows that the case of (i) $\lambda = 0$, or non-zero and positive, (ii) non-zero and negative can be distinguished this way, as explained in Table III. On the other hand, the sign of $\delta\kappa_\gamma$ can be distinguished in the absence of λ_γ , whereas it is hard to do this if λ_γ is non-zero. At $\sqrt{s} = 500$ GeV, with 100 fb^{-1} luminosity, the bound on the λ_γ , when it is negative could be improved by about a factor of 2 by considering the forward-backward asymmetry at a fixed energy (E_μ), compared to the case when the energy is integrated out.

We are aware that the present considerations of the ILC do not favour a photon collider option as priority. At the same time, we hope that this study will help the case for this option at ILC, and expect it to be available eventually. Meanwhile, although more accurate estimates incorporating collider and detector effects, and beam polarization effects are needed to make more quantitative conclusions, we hope our analyses has shown that the leptonic decay of the W produced in $e\gamma$ collision is one of the neat and simple process to probe the $WW\gamma$ coupling without the complications of other couplings. Further, the process has the potential to probe the couplings to a few per-mil level with suitably constructed observables, which could also be used to distinguish different scenarios involving the two parameters, $\delta\kappa_\gamma$ and λ_γ .

Acknowledgment:

PP's work is partly supported by a BRNS, DAE, Government of India (Project No.: 2010/37P/49/BRNS/1446).

Appendix: Photon luminosity distribution

The colliding photons in a realistic electron-photon collider does not have a fixed energy, rather the beam will have distribution of photons with energy varying over an allowed range (which depends on the initial electron and laser photon energies among other things). In such colliders, the cross-section and other observables should, therefore, be properly folded with a luminosity distribution function to get the measurable quantities, as is done in Eq. 12.

At ILC high energy, high luminosity photon beam is obtained by Compton backscattering of low energy, high intensity laser beam off high energy electron beam. Ideal Compton backscattered photon spectrum is given by [29–31]

$$f_{\gamma/e}(x) = \frac{1}{D(\xi)} \left[1 - x + \frac{1}{1-x} - 4 \frac{x}{\xi(1-x)} + 4 \frac{x^2}{\xi^2(1-x)^2} \right]$$

$$D(\xi) = \left(1 - \frac{4}{\xi} - \frac{8}{\xi^2} \right) \ln(1+\xi) + \frac{1}{2} + \frac{8}{\xi} - \frac{1}{2(1+\xi)^2}, \quad (11)$$

where $x = \frac{\omega}{E_e}$, with E_e the energy of the initial electron and ω the energy of the scattered photon. x thus gives the fraction of the electron energy carried by the scattered photon. Dependence of the distributions on the initial laser photon energy (ω_0) comes through $\xi \approx \frac{4E_e\omega_0}{m_e^2}$, where m_e is the electron mass. The maximum value of x is $x_{max} = \frac{\xi}{1+\xi}$. It is, but not possible to increase ω_0 and E_e to any value to get larger x_{max} . It is found that for ξ beyond ~ 4.8 , conversion efficiency drops down drastically due to e^+e^- pair production between the laser photons and the backscattered photons, setting an absolute upper limit on $x \approx 0.83$. This value essentially means that with an electron beam of energy $E_e = 250$ GeV, we can effectively go up to $\omega_0 \approx 1.26$ eV.

For an $e\gamma$ collider, the luminosity factor (Eq. 12) is the same as the above energy spectrum:

$$\frac{d\mathcal{L}_{\gamma/e}(x)}{dx} = f_{\gamma/e}(x) \quad (12)$$

In a realistic collider, one need to also worry about many detailed aspects, like the non-linear effects making the actual photon spectrum deviating from the ideal case in Eq. 11, the polarization

of the hard photon. The polarization (P_γ) of the scattered photon itself depend on the initial electron (P_e) and the laser beam polarization (P_l). In the high energy region, it is noted that $P_\gamma = -P_e$ [29–31]. This could be used to the advantage of the physics studies being considered. In our analysis, we have not gone into these details. we have assumed unpolarized initial electron and laser beams, which produces an unpolarized high energy photon beam (to a very good approximation).

For more details on photon collider one may refer to Ref. [29–31, 33] and references therein.

-
- [1] G. Aad *et al.* [ATLAS Collaboration], Phys. Lett. B **716**, 1 (2012) [arXiv:1207.7214 [hep-ex]].
 - [2] G. Aad *et al.* [ATLAS Collaboration], Phys. Lett. B **726** (2013) 88 [arXiv:1307.1427 [hep-ex]].
 - [3] S. Chatrchyan *et al.* [CMS Collaboration], Phys. Lett. B **716**, 30 (2012) [arXiv:1207.7235 [hep-ex]].
 - [4] S. Chatrchyan *et al.* [CMS Collaboration], JHEP **1306** (2013) 081 [arXiv:1303.4571 [hep-ex]].
 - [5] S. Dawson, Introduction to EWSB, (arXiv:hep-ph/9901280v1, 12 Jan 1999).
 - [6] A. Djouadi, Phys. Rept. **457** (2008) 1 [hep-ph/0503172].
 - [7] W. Buchmuller and C. Ludeling, hep-ph/0609174.
 - [8] T. Corbett, O. J. P. Boli, J. Gonzalez-Fraile and M. C. Gonzalez-Garcia, Phys. Rev. Lett. **111** (2013) 011801 [arXiv:1304.1151 [hep-ph]].
 - [9] J. Gonzalez-Fraile, arXiv:1411.5364 [hep-ph].
 - [10] J. Brau *et al.* [ILC Collaboration], arXiv:0712.1950 [physics.acc-ph]; G. Aarons *et al.* [ILC Collaboration], arXiv:0709.1893 [hep-ph].
 - [11] D. M. Asner, T. Barklow, C. Calancha, K. Fujii, N. Graf, H. E. Haber, A. Ishikawa and S. Kanemura *et al.*, arXiv:1310.0763 [hep-ph].
 - [12] K. Moning, J. Sekaric, Eur. Phys. J. C **38**, 427-436 (2005).
 - [13] S. J. Brodsky, T. G. Rizzo and I. Schmidt, Phys. Rev. D **52**, 4929 (1995) [arXiv:hep-ph/9505441].
 - [14] M. A. Doncheski, S. Godfrey and K. A. Peterson, arXiv:hep-ph/9710299; M. A. Doncheski, S. Godfrey and K. A. Peterson, Phys. Rev. D **59**, 117301 (1999).
 - [15] E. M. Gregores, M. C. Gonzalez-Garcia and S. F. Novaes, Phys. Rev. D **56**, 2920 (1997) [arXiv:hep-ph/9703430].
 - [16] K. Ackerstaff *et al.* [OPAL Collaboration], Eur. Phys. J. C **2**:597-606 (1998).
 - [17] E. Yehudai Phys. Rev. D **44**, 3434 (1991).
 - [18] G. J. Gounaris, J. Layssac and F. M. Renard, Z. Phys. C **69**, 505 (1996) [arXiv:hep-ph/9505430].
 - [19] K. Hagiwara, R. D. Peccei, D. Zeppenfeld and K. Hikasa, Nucl. Phys. B **282**, 253 (1987).
 - [20] J. Alcaraz *et al.* [ALEPH Collaboration and DELPHI Collaboration and L3 Collaboration and OPAL Collaboration and LEP Electroweak Working Group], arXiv:hep-ex/0612034.
 - [21] S. Schael *et al.* [ALEPH and DELPHI and L3 and OPAL and LEP Electroweak Collaborations], Phys. Rept. **532**, 119 (2013) [arXiv:1302.3415 [hep-ex]].
 - [22] V. M. Abazov *et al.* [D0 Collaboration], Phys. Rev. Lett. **100**, 241805 (2008) [arXiv:0803.0030 [hep-ex]].
 - [23] S. Chatrchyan *et al.* [CMS Collaboration], Phys. Lett. B **701** (2011) 535 [arXiv:1105.2758 [hep-ex]].
 - [24] S. Atag and I. Sahin, Phys. Rev. D **75**, 073003 (2007) [arXiv:0703201 [hep-ph]].
 - [25] I. Sahin and A. A. Billur, Phys. Rev. D **83**, 035011 (2011) [arXiv:1101.4998 [hep-ph]]; E. Chapon, C. Royon and O. Kepka, Phys. Rev. D **81**, 074003 (2010) [arXiv:0912.5161 [hep-ph]].
 - [26] E. Yehudai, Phys. Rev. D **41**, 33 (1990); S. Y. Choi, J. S. Shim, H. S. Song, J. Song and C. Yu, Phys. Rev. D **60**, 013007 (1999) [arXiv:hep-ph/9901368]; M. Gintner, S. Godfrey and G. Couture, Phys. Rev. D **52** (1995) 6249 [arXiv:hep-ph/9511204]; H. Aihara *et al.*, arXiv:hep-ph/9503425; G. Couture and S. Godfrey, Phys. Rev. D **50**, 5607 (1994) [arXiv:hep-ph/9406257]; Mamta Dahiya, Sukanta Dutta, Rashidul Islam, arXiv:1311.4523 [hep-ph].
 - [27] J. A. M. Vermaseren, arXiv:math-ph/0010025.
 - [28] T. Hahn, Comput. Phys. Commun. **168**, 78 (2005) [hep-ph/0404043].
 - [29] I. F. Ginzburg *et al.*, Nucl. Instrum. Methods, **205**, 47 (1983); 219, 5 (1984).
 - [30] V. I. Telnov, arXiv:0908.3136 [physics.acc-ph].
 - [31] M. M. Muhlleitner and P. M. Zerwas, Acta Phys. Polon. B **37**, 1021 (2006) [arXiv:hep-ph/0511339].
 - [32] J. Beringer *et al.*, (Particle Data Group), Phys. Rev. D **86**, 010001 (2012).
 - [33] G. Moortgat-Pick, T. Abe, G. Alexander, B. Ananthanarayan, A. A. Babich, V. Bharadwaj, D. Barber and A. Bartl *et al.*, Phys. Rept. **460** (2008) 131 [hep-ph/0507011].